frontiers | Frontiers in Materials

TYPE Original Research
PUBLISHED 18 May 2023
DOI 10.3389/fmats.2023.1188411

OPEN ACCESS

EDITED BY
Guosong Wu,
Hohai University, China

REVIEWED BY
Lin Mao,
University of Shanghai for Science and Technology, China
Qing Ouyang,
Jiaxing University, China

*CORRESPONDENCE
Haoliang Lv,
lhl801@qq.com
Zhaomeng Chen,
chernzm@szpt.edu.cn

RECEIVED 17 March 2023
ACCEPTED 05 May 2023
PUBLISHED 18 May 2023

CITATION
Lv G, Lv H, Chen Z, Chu W and Mao J (2023), Research on inertia transfer in load simulation of tracked vehicle under complex working conditions.
Front. Mater. 10:1188411.
doi: 10.3389/fmats.2023.1188411

Research on inertia transfer in load simulation of tracked vehicle under complex working conditions

Gang Lv[1], Haoliang Lv[2]*, Zhaomeng Chen[3]*, Wei Chu[1] and Jiliang Mao[2]

[1]School of Mechanical and Electrical Engineering, Xi'an University of Architecture and Technology, Xian, Shaanxi, China, [2]Suzhou Sc-Solar Equipment Co., Ltd., Suzhou, Jiangsu, China, [3]School of Automotive and Transportation Engineering, Shenzhen Polytechnic, Shenzhen, China

At present, research on the loading simulation test bench for overloaded vehicles is mostly limited to the realization of loading simulation under the condition of straight line driving of the vehicle. When simulating the whole vehicle load under straight line driving condition, only accurate road load and inertial load can be obtained to achieve accurate load simulation, and the inertial load required to be simulated by each side device is half of the whole vehicle inertial load. However, straight line driving is only the most ideal driving. The real driving conditions (including ground conditions) of the vehicle are usually composed of steering, longitudinal slope, lateral slope and different ground adhesion coefficients. Therefore, the loads borne by the two independent load simulation systems located on both sides of the vehicle may be different during the load simulation process. In addition, the frequency characteristics of the loads to be simulated by the same side load simulation device at different time sequences may also be different. This paper studies the dynamics modeling, load distribution and error compensation in the whole vehicle load simulation process in order to achieve accurate crawler vehicle load simulation from three aspects.

KEYWORDS

tracked vehicles, load simulation, complex working conditions, load distribution, testing technology

1 Introduction

In the actual driving process of tracked vehicles, the vehicle and its driven and transmission parts are affected by external factors such as inertia load, wind resistance, slope resistance, etc., in real time. These influencing factors are constantly changing in an unordered manner as the vehicle travels. In the bench test, since the test piece is fixed and immovable, these factors cannot be reflected. Therefore, the running resistance of the test piece in the bench test is different from the real situation. In order to ensure the authenticity and accuracy of the load simulation on the test bench, compensation loading needs to be applied to the test pieces running on the test bench, and the core technology for achieving compensation loading is the load simulation technology (Fajri et al., 2013; Yang et al., 2013; Takeda et al., 2014).

Accurate load simulation is premised on having an accurate vehicle load model. The load on the drive system during the vehicle's journey can be divided into road load and inertial load. The road load of the vehicle is formed by the gravity of the vehicle, the driving

conditions of the vehicle, the ground conditions, etc. In the discussion of road load, the changes in the load on the left and right wheels under different driving conditions need to be considered. For tracked vehicles, the distribution of the load on the ground where the track is in contact needs to be taken into consideration.

In reference Xingguo et al. (2011), dynamics analysis and discussion of tracked vehicles were conducted by using multi-body dynamics software, and vehicle models applicable to different roads were obtained by modeling and simulation based on different road models. This provides a theoretical basis for the performance analysis of the whole vehicle and vehicle components. In reference Bai et al. (2017) and others, in order to study the dynamic load characteristics of the multi-axis vehicle powertrain system, a dynamic simulation model of the multi-axis vehicle powertrain system was established. The author established the dynamic simulation model of the transmission system including the hydraulic torque converter, clutch, differential, differential, main reducer, wheel side reducer, etc., and established the dynamic simulation model of the multi-axis vehicle powertrain system in Simulink. The comparison results of simulation and experimental data show that the model can effectively simulate the dynamic load characteristics and speed characteristics. The inertial load is the load formed by the inertia of the whole vehicle during the acceleration process. When establishing a wheeled vehicle dynamic model using traditional methods, the coefficients of the rotating components (such as wheels and transmission systems) and the equivalent inertia of the output shaft are estimated to calculate the body inertia, which is then equivalent to the output shaft (Kim et al., 2003; Fu et al., 2009; Wang et al., 2018). In the modeling process of general light-load vehicles, the kinetic energy of the rotating components and the slip rate between the vehicle and the ground are basically ignored. Due to the ratio of the mass of the rotating part to the total mass of the wheeled vehicle being very small, the estimation error of the equivalent mass is very small.

In reference Ott et al. (2021), a multibody system was used, which consists of five bodies. By applying methods of multibody modelling the generalized equations of motion were generated. To include the behavior within the contact point between road and vehicle a simplified tire models was added. The model was simulated numerically to investigate different load states of the vehicle, by applying constant steering stimuli and variable velocities. In reference ChenZhouWang et al. (2019), in order to study the braking performance of electric tracked vehicles, the vehicle ground contact state under straight driving conditions was analyzed, a vehicle slip rate model was established, and fuzzy control algorithm was used to simulate the synchronous load on both sides of the vehicle. In reference Jiang et al. (2022), a three-degree-of-freedom vehicle dynamics model is established accurately, a rollover evaluation index and a safety threshold are selected quickly, and the working principle and detailed control scheme of the motor speed control strategy are given. In order to achieve stable control of vehicle driving in a straight direction, reference (Lv et al., 2019) proposed a 2-degree-of-freedom (2-DOF) control method combined with a disturbance observer to solve the stability problem of the system. The test results show that the system has a high load simulation accuracy under various load simulation tests.

Heavy-duty vehicles have different modeling of equivalent inertia due to their special structure (Huh et al., 2001; Zou et al., 2016). Taking tracked vehicles as an example, the rotating parts of tracked vehicles include parts with a large proportion of vehicle weight, such as tracks (Wang and Sun, 2014). If the same calculation method as wheeled vehicles is adopted, a larger error will be produced. Therefore, in the process of heavy-duty vehicle load simulation, different forms of modeling must be carried out for different vehicles to ensure the accuracy of the model.

According to the current research progress, there are two problems in the research of vehicle load:

1) When establishing the road load model of the vehicle, the driving condition is relatively simple, which cannot accurately reflect the load and its distribution of the vehicle under general driving conditions;
2) Lack of in-depth research on the equivalent inertia of tracked vehicles, and lack of research on the distribution of equivalent inertia of ground slip rate, left and right driving wheels in the modeling process.

To address the above issues, this article establishes a dynamic model for the complex driving process of the entire vehicle, considers the load distribution of the vehicle under various operating conditions, and establishes the accurate equivalent inertia of the vehicle during the load simulation process. The inertia torque formula is used to achieve the load simulation of the vehicle. To improve the load simulation accuracy of the vehicle, a form of cross coupling error compensation is proposed to reduce the error of the simulation device.

2 Research on whole vehicle road load model

The road load on the whole vehicle during its running process is derived from the energy loss of wheel/track ground friction, slope resistance and resistance generated by ground deformation. Due to the interaction of various forces such as slope resistance, steering resistance and centrifugal force during the running process of the vehicle, the road load on the vehicle is different in different running states. This section takes tracked vehicles as an example to analyze their kinematics and dynamics, and explore the road load of the vehicle under different driving conditions.

2.1 Principle of load simulation

In the process of vehicle load simulation, the test bench needs to reproduce the actual working conditions of the vehicle on the actual road surface, that is, the bench needs to respond to both the torque output of the vehicle's driving system and the speed output of the vehicle (Nam, 2001). It can be seen that the load simulated by the motor in the load simulation system is determined by the output of the vehicle's driving wheel. The principle of load simulation is shown in Figure 1:

The tested vehicle in Figure 1 is controlled by the driver's behavior, outputting speed and torque. After the speed and

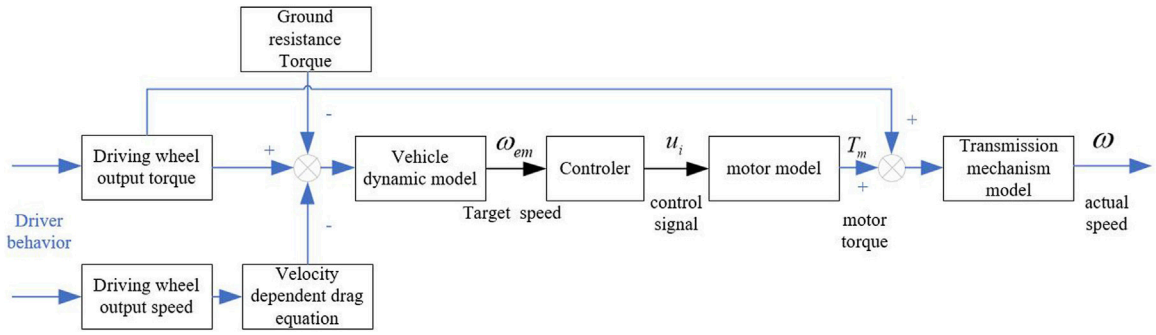

FIGURE 1
Load simulation schematic diagram.

torque signals are obtained by the sensor, the target speed of the system is obtained through the superposition with the resistance torque and the vehicle dynamics model. The target speed is converted into an electrical signal, which is then converted into the motor output torque through the controller and motor transfer function model. The output torque of the motor and the output torque of the vehicle's driving wheel jointly act on the transmission mechanism, allowing the transmission mechanism to output the actual speed to achieve load simulation of the entire vehicle.

As shown in Figure 1, in order to accurately reproduce the rotational speed output of the entire vehicle, it is necessary to obtain the accurate equivalent inertia of the entire vehicle equivalent to the driving wheel. According to the formula for balancing the driving force of the entire vehicle, assuming that the torque output from the driving system to the driving wheel under a certain working condition is T_e, the road load is converted into the torque on the driving wheel and the torque balance is calculated:

$$T_e = T_a + T_s + T_w + T_f \tag{1}$$

In the formula, T_s、 T_w、 T_f correspond to the torque of the entire vehicle's slope resistance, wind resistance, and rolling resistance on the driving wheel respectively. T_a is the inertia moment exerted by the inertia force of the entire vehicle on the driving wheel.

During the actual road driving process of a vehicle, the body motion is divided into two parts: translational and rotational. Assuming that the translational part of the vehicle is a rigid block with a mass of m_v and a moving speed of v_v, the inertia of the rotating part of the vehicle around its center of rotation is $J_i\,(i = 1, 2, \cdots)$ and the rotational speed is $\omega_i\,(i = 1, 2, 3\cdots)$. The inertia load of the entire vehicle can be expressed as:

$$\frac{T_a}{R} = m_v v_v + J_i \omega_i\,(i = 1, 2, 3, \cdots) \tag{2}$$

At this point, the relationship between v_v and ω_i can be obtained by converting the inherent structure of the vehicle body and the operating state of the entire vehicle. When the whole vehicle model is transferred from the actual road surface to the test bench, because the translation acceleration, track acceleration and wheel angular acceleration of the whole vehicle are all reflected on the driving wheel by the angular acceleration of the driving wheel, the mass of the whole vehicle, track mass and wheel inertia need to be equivalent to the driving wheel, namely:

$$T_a = r_d\,(m_v v_v + J_i \omega_i) = J_{equ}\dot{\omega}_d \tag{3}$$

Where J_{equ} is the equivalent inertia of the entire vehicle on the driving wheel, and $\dot{\omega}_d$ is the first-order derivative of the driving wheel speed.

During the driving process of the vehicle, the inertia resistance and road resistance experienced by the entire vehicle are transmitted to the vehicle drive system in the form of loads through the wheels. Assuming that the effective working radius of the wheels is R, the torque T on the half axle is:

$$T = FR = J_{equ} a_d \tag{4}$$

Substitute Eq. 3 into Eq. 4 and perform Laplace transformation to obtain:

$$G_{em} = \frac{\omega_d}{T_e(s) - T_s(s) - T_w(s) - T_f(s)} = \frac{1}{J_{equ} s} \tag{5}$$

Where G_{em} is the transfer function with the force on the driving wheel as the input and the speed of the driving wheel as the output, that is, the vehicle dynamics model. In Eq. 6, define:

$$T_s(s) + T_w(s) + T_f(s) = T_l(s) \tag{6}$$

Then $T_l(s)$ is the ground/air resistance torque during vehicle operation. Therefore, the working principle of the load simulation system is to match the system with the actual working condition by simulating the ground/air resistance moment $T_l(s)$ when the driving force $T_e(s)$ and equivalent inertia J_{equ} are given.

According to Eq. 5 and Eq. 6, from the perspective of discrete domain analysis, with known equivalent inertia J_{equ}, input torque $T_e(i)$, and active wheel speed $\omega_d(i)$ of the vehicle at time i, the vehicle's rotational speed at time $(i + \Delta i)$ is:

$$\omega_d(i + \Delta i) = \frac{T_e(i) - T_l(i)}{J_{equ}} \times \Delta i + \omega_d(i) \tag{7}$$

Meanwhile, the load simulation system consists of a load motor and a mechanical transmission system. From the perspective of force acting on the test bench, the torque balance equation of the bench is:

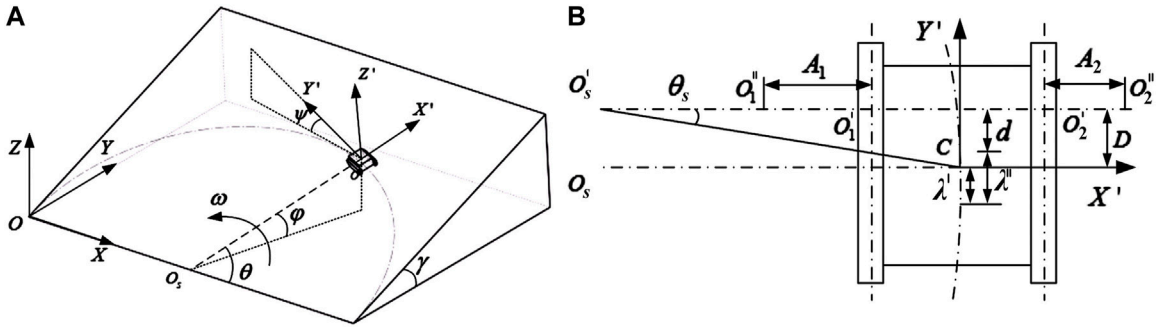

FIGURE 2
(A) The instantaneous posture of the vehicle when turning on a certain slope; **(B)** Kinematic analysis of X′O′Y′ plane motion during vehicle travel.

$$T_e = T_r + T_d + Ja_r \tag{8}$$

Wherein, T_r is the load torque of the load simulation system acting on the driving wheel, T_d is the rotating resistance loss of the test bench (including viscous resistance, friction resistance, etc.) synthesized by various factors, J is the mechanical inertia of the rotating part of the test bench, and a_r is the angular acceleration of the output shaft of the test bench.

When the vehicle carries out the load simulation test according to the method in Figure 1, it can be seen that $a_d = a_r$, that is, the actual angular acceleration of the wheels when the vehicle is running on the road is equal to the angular acceleration of the bench. At this point, substituting Eq. 8 into Eq. 1 yields:

$$T_r = T_f + T_w + \left(J_{equ} - J\right)a_d \tag{9}$$

According to the above equation, in order to accurately achieve the load simulation function of the platform, it is necessary to obtain an accurate road load model $T_l(s)$, equivalent inertia model J_{equ}, transfer function model $G_m(s)$ of the load motor, and transfer function model $G_j(s)$ of the mechanical system.

2.2 Analysis of the vehicle's kinematics

Currently, the kinematics and dynamics of the whole vehicle of tracked vehicles are usually studied in terms of steering motion in the horizontal plane or straight line motion on a slope (Yalla et al., 2007; Janarthanan et al., 2011). This type of working condition can only represent part of the working conditions during the vehicle's travel. In order to comprehensively study the kinematics and dynamics of the vehicle under the load working condition, this section establishes the vehicle motion coordinate system shown in Figure 2A. Assuming that the tracked vehicle is traveling on a slope with an inclination angle of γ, let the world coordinate system of the slope be *O-XYZ*, the body coordinate system be $O' - X'Y'Z'$, and the body center of mass be *C*. $O'$and C coincide in the world coordinate system. At a certain moment, the vehicle takes O_s as the steering center, l_{O_sC} as the steering radius, and the angular velocity ω rotates uniformly around O_s for θ degrees.

At this moment, according to Figure 2A, the instantaneous side tilt angle φ of the body in the $X'O'Z'$ plane can be obtained.

$$sin\,\varphi = sin\,\gamma \cdot sin\,\theta \tag{10}$$

The instantaneous pitch angle Ψ of the body in the $Y'O'Z'$ plane can be obtained.

$$tan\,\Psi = tan\,\gamma \cdot cos\,\theta \tag{11}$$

The components of the weight of the vehicle in the $O' - X'Y'Z'$ coordinates can be expressed in vector form:

$$G' = -mg\left[sin\,\gamma\,sin\,\theta\,sin\,\gamma\,cos\,\theta\,cos\,\gamma\right]^T \tag{12}$$

Analysis of the motion of the vehicle in the $X'O'Y'$ plane is conducted, assuming that the vehicle travels at a constant speed around the steering center O_s with a steering radius $l_{O_sC} < \infty$, and under the influence of the pitch angle Ψ, the steering center of the vehicle in contact with the ground must deviate from the *O* point in the negative direction of Y' by a distance λ'. At the same time, due to the existence of the tilt angle φ, the steering center of the vehicle to the ground must be offset from *O* to the positive direction of *Y* by a distance λ'' (see Section 2.3 for detailed derivation). At this time, the direction of the track winding speed points to the tangent direction of the whole vehicle steering direction, and the absolute speed direction of the track parallel to the winding speed direction only exists at the geometric center O_1, O_2 of the two sides of the track. At other positions, the track ground element must inevitably slip relative to the ground. According to Figure 2B, it can be seen that at a certain moment when the vehicle is turning, the speed of the track at the instantaneous center O_1'', O_2'' is compared with the original geometric center O_1', O_2', respectively offset by A_1, A_2 in the X' direction and d in the longitudinal direction. Furthermore, when the vehicle is in high-speed motion, the offset distance *D* formed by the superposition of λ'、 λ'', and d causes a lateral deviation angle θ_s between the direction of the centrifugal force passing through the vehicle's center of mass and the X' axis direction, and the centrifugal force further counteracts on λ'、 λ'' in the X′ and Y' directions, respectively. Therefore, the kinematic process of vehicle steering is the process of interaction between v_v、 λ'、 λ'' and *d*.

The traction speed of the center line of the track on both the inside and outside when the tracked vehicle is turning is:

$$v_{o'i} = \left(l_{O_s'} \pm \frac{B}{2}\right)\omega \ (i = 1, 2) \tag{13}$$

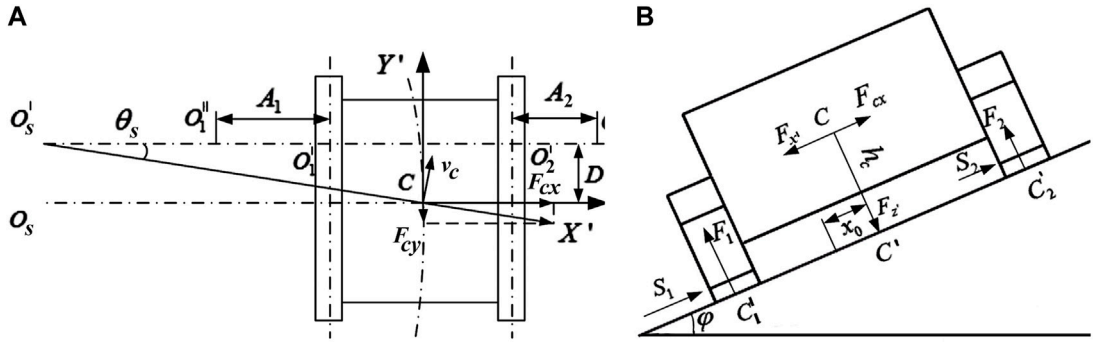

FIGURE 3
(A) Dynamics analysis of X′O′Y′ plane during vehicle travel; **(B)** X′O′Z′ mechanics analysis during vehicle travel.

Where B is the width of the vehicle; ω is the angular velocity of the vehicle; $l_{O_s'}$ is the lateral distance from the actual steering center to the center of gravity of the body, that is, $l_{O_s'} = l_{O_s'C}\cos\theta_s$, $l_{O_s'C}$ is the actual steering radius.

In the process of motion analysis, assuming that the ground contact of the tracks is all concentrated on the center line O_1'、O_2', the relative line speed of the two tracks is:

$$\left(l_{O_s'} \pm \frac{B}{2} + A_i\right)\omega = v_{qi}\,(i = 1, 2) \tag{14}$$

The slip rate of the tracks on both sides inside and outside can be expressed by the following equation:

$$\delta_i = \frac{v_{qi} - v_{o'i}}{v_{qi}}\,(i = 1, 2) \tag{15}$$

According to Figure 2B:

$$l_{O_s'C} = \sqrt{l_{O_s'}^2 + D^2} = \sqrt{\left(\frac{\frac{B}{2}\left(v_{q2} + v_{q1}\right) + A_2 v_{q1} - A_1 v_{q2}}{v_{q2} - v_{q1}}\right)^2 + D^2} \tag{16}$$

Further deducted, it can be obtained as:

$$\delta_i = \frac{A_i}{l_{O_s'} \pm \frac{B}{2} + A_i}\,(i = 1, 2) \tag{17}$$

2.3 Vehicle dynamics analysis

Analysis of the forces on the vehicle in the $X'OY'$ plane yields the force model shown in Figure 3A. At this time, due to the vehicle's center of mass C revolving around the actual instantaneous steering center O', a centrifugal force $F_c = mv^2/R$ is generated, and the components of the centrifugal force in the X'、Y' directions are respectively:

$$\begin{cases} F_{cx} = \dfrac{mv^2}{R}\cos\theta_d \\ F_{cy} = \dfrac{mv^2}{R}\sin\theta_d \end{cases} \tag{18}$$

In the $X'O'Z'$ plane, due to the existence of the side tilt angle φ, the vehicle is simultaneously subjected to the normal ground support force F_i, lateral resistance S_i $(i = 1, 2)$, centrifugal force F_{cx}, and the combined effect of gravity, as shown in Figure 3B.

According to the above figure, the ground reaction forces of the left and right tracks can be obtained by calculating the moment at points C_1'、C_2':

$$\begin{cases} F_1 = \dfrac{mg\cos\gamma}{2} + \dfrac{h_c}{B}\left(mg\sin\gamma\sin\theta - \dfrac{mv^2\cos\theta_s}{R}\right) \\ F_2 = \dfrac{mg\cos\gamma}{2} - \dfrac{h_c}{B}\left(mg\sin\gamma\sin\theta - \dfrac{mv^2\cos\theta_s}{R}\right) \end{cases} \tag{19}$$

Therefore, the center of the ground support reaction along the X′ direction is offset by:

$$x_0 = \frac{h_c\left(g\sin\gamma\sin\theta - \frac{v^2\cos\theta_s}{R}\right)}{g\cos\gamma} \tag{20}$$

In the $Y'O'Z'$ plane, due to the existence of the slope angle Ψ, the center of the ground support force has an offset y_0 from the geometrical center C' of the track ground contact. At this time, the change of the whole vehicle planar load distribution caused by the elevation angle Ψ is shown in Figure 4A.

When a tracked vehicle turns on a horizontal plane, the combined force of the ground reaction force and the pressure center of the track contacting the ground coincide. When the vehicle is running on a slope, the ground counteraction force provided to the track can be decomposed into the vertical support force $mgcos\alpha$ and the sliding force $F_{y'} = mgsin\alpha\cos\beta$ parallel to the slope, and the vehicle is subjected to the centrifugal force component F_{cy} caused by the steering side slip angle θ_s in the Y' direction. Without considering the lateral force, the center of the normal reaction force $F_{z'}$ of the ground and the geometric center C' of the track-ground contact have a bias distance y_0 in the Y' direction. Assuming that the vehicle is running stably at this time, the torque balance equation of the vehicle at C' is obtained.

$$h_c\left(mg\sin\gamma\cos\theta + \frac{mv^2\sin\theta_s}{R}\right) = y_0 mg\cos\gamma \tag{21}$$

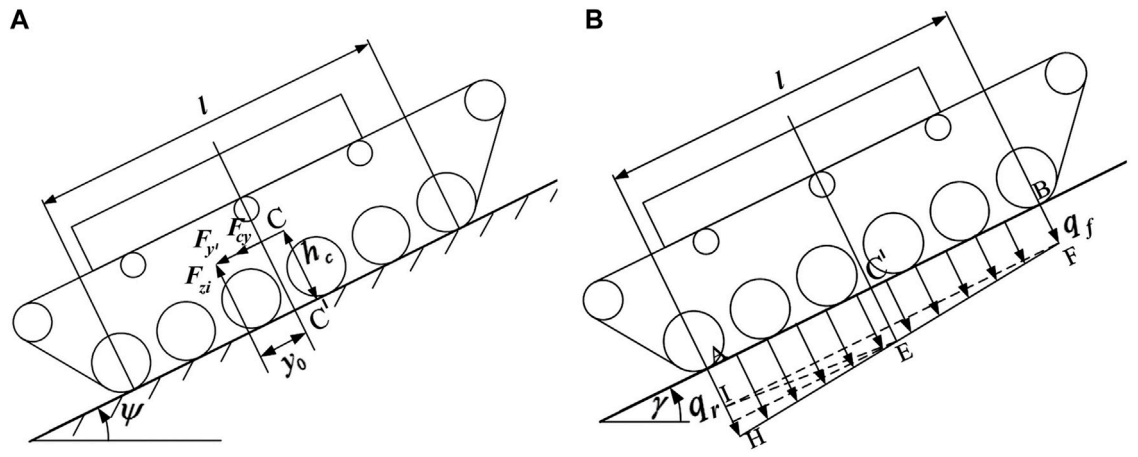

FIGURE 4
(A) Whole vehicle plane force analysis; **(B)** Analysis of normal load of track ground contact.

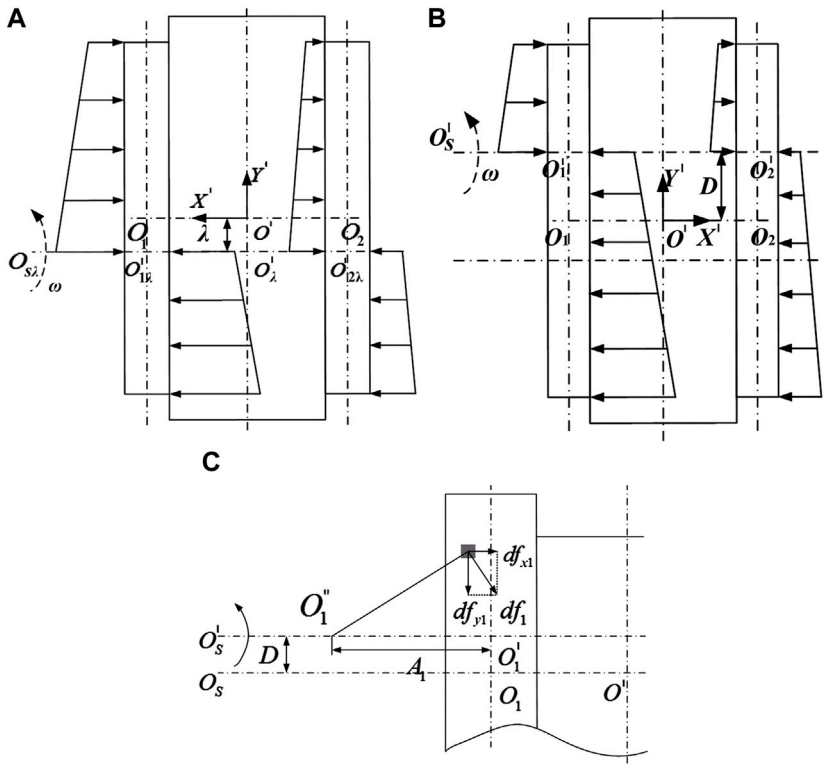

FIGURE 5
(A) Vehicle lateral force model without considering slip and yaw; **(B)** Vehicle lateral force model considering slip and yaw; **(C)** Analysis of the force on the inner track contacting the ground during the steering process.

Then it is easy to get the expression of the bias distance y_0 according to the above equation:

$$y_0 = h_c \cdot \tan\gamma \cdot \cos\theta + \frac{v^2 \sin\theta_s}{Rg\cos\gamma} \tag{22}$$

Due to the offset of the normal force center of the ground, the normal load of the track contacting the ground changes from rectangular to trapezoidal at this time. The unit length normal load at the front end is q_f, the unit length normal load at the rear end is q_r, and the average unit length normal load is q_a, as shown in Figure 4B.

According to Figure 4B, $q_{ai} = \frac{1}{2}(q_f + q_r) = F_i\ (i = 1, 2)$, the torque balance equation at point C' can be obtained as follows:

$$M_{ABFH} = y_0 mg\cos\gamma \tag{23}$$

$$M_{IEH} = \int_0^{\frac{L}{2}} \frac{2(q_r - q_f)}{L} l^2 dl \tag{24}$$

Then it can be obtained:

$$\begin{cases} q_f = q_a\left(1 - \dfrac{6y_0}{L}\right) \\ q_r = q_a\left(1 + \dfrac{6y_0}{L}\right) \end{cases} \tag{25}$$

Further it can be obtained:

$$\begin{cases} q_1(x, y) = \dfrac{F_1}{bL}\left(1 - \dfrac{12(y+d)}{L^2}h_c \cdot \tan\gamma \cdot \cos\theta - \dfrac{12(y+d)}{L^2}\dfrac{v^2 \sin\theta_s}{Rg\cos\gamma}\right) \\ q_2(x, y) = \dfrac{F_2}{bL}\left(1 - \dfrac{12(y+d)}{L^2}h_c \cdot \tan\gamma \cdot \cos\theta - \dfrac{12(y+d)}{L^2}\dfrac{v^2 \sin\theta_s}{Rg\cos\gamma}\right) \end{cases} \tag{26}$$

Due to the longitudinal component F_{cy} of the centrifugal force and the component $F_{y'}$ of the total vehicle weight along the direction of travel, the pressure at the front end of the track contact section is reduced and the rear end is increased, so the steering resistance moment of the vehicle is distributed in a trapezoidal shape with a small front and a large rear, as shown in Figure5A. Simultaneously, due to the influence of the slope angle φ and the tilt angle Ψ, the instantaneous rotation center of the vehicle is offset in the Y' direction from the vehicle's center of mass by a distance of λ.At the same time, during the vehicle steering process, due to the sliding/rolling of the track, the speed of the track will instantaneously produce offset A_1、A_2 in the X′ direction, and eventually cause an offset of size D in the Y' direction of the steering center. Under the condition of considering the offset of the steering center, the lateral resistance distribution of the track to the ground is shown in Figure 5B.

A force analysis model of the ground contact element of the track has been established in the $O' - X'Y'Z'$ coordinate system. Taking a microelement with a length and width of (dx, dy) on the track ground, the friction force of the ground microelement and the ground in the X'、 Y' directions are shown in Figure 5C.

It can be obtained that the force on each contact ground element in the X'、Y' directions is respectively:

$$\begin{cases} df_{xi} = \mu_x q_i(y_i)\sin\theta \\ df_{yi} = \mu_y q_i(y_i)\cos\theta \end{cases} (i = 1, 2) \tag{27}$$

In the equation, μ_x、 μ_y are the friction coefficients of the caterpillar touching the ground, and the friction coefficient is affected by the caterpillar's sliding rate, which is expressed as

$$\begin{cases} \mu_x = E_1\left(1 - e^{-E_2}\right) \\ \mu_y = E_1\left(1 - e^{-E_2|\delta_i|}\right) \end{cases} \tag{28}$$

In the equation, E_1、 E_2 are design constants determined by the sliding test.

Further derivation of Eq. 27 can obtain the friction resistance components in the X'、Y' axes generated by the contact surface between the track and the ground, as well as the steering resistance moment generated by the ground to the track, respectively:

$$\begin{cases} F_{xi} = \iint df_{xi}dxdy = \int_{A_i-\frac{b}{2}}^{A_i+\frac{b}{2}} dx \int_{-\frac{L}{2}-d_i}^{\frac{L}{2}-d_i} \mu_x q_i(y_i)\dfrac{y}{\sqrt{x^2+y^2}}dy \\ F_{yi} = \iint df_{yi}dxdy = \int_{A_i-\frac{b}{2}}^{A_i+\frac{b}{2}} dx \int_{-\frac{L}{2}-d_i}^{\frac{L}{2}-d_i} \mu_y q_i(y_i)\dfrac{x}{\sqrt{x^2+y^2}}dy \quad \mathrm{i} = (1, 2) \\ M_{ri} = \iint\left((y+d_i)f_{xi} - (A_i - x)f_{yi}\right)dxdy = \int_{A_i-\frac{b}{2}}^{A_i+\frac{b}{2}} dx \int_{-\frac{L}{2}-d_i}^{\frac{L}{2}-d_i} \mu_y q_i(y_i)\dfrac{x(x-A_i)+y(y+d_i)}{\sqrt{x^2+y^2}}dy \end{cases} \tag{29}$$

According to D'Alembert's principle, the force balance equation of the vehicle can be obtained in the relative coordinate system $O' - X'Y'Z'$.

$$\begin{cases} m_v\ddot{x} = F_{x1} + F_{x2} - F_{x'} \\ m\ddot{y} = F_{y1} + F_{y2} - F_{r1} - F_{r2} - F_{y'} - \dfrac{C_D A}{21.25}v_v \\ J_{z'}\dot{\omega} = M_{r1} + M_{r2} + \dfrac{B}{2}\left(F_{y2} + F_{r1} - F_{y1} - F_{r2}\right) \end{cases} \tag{30}$$

In the equation, F_{ir} $(i = 1, 2)$ represents the ground resistance of the vehicle, and according to the theory of ground-track bearing (Wang et al., 2015), we can obtain:

$$F_{ir} = \frac{1}{(\mathrm{n}+1)\left(k_c + bk_\varphi\right)^{1/n}}\left(\frac{F_i}{bl}\right)^{(n+1)/n} \tag{31}$$

In the equation, k_c is the soil cohesion modulus, k_φ is the soil friction modulus, n is the soil deformation index, which changes with different soil components, water content and other conditions, and is a constant independent of external conditions such as pressure and contact surface.

Substituting Eq. 29 into Eq. 30, it can be seen that the equation set listed has hidden unknown motion parameters, and there is a coupling relationship between the parameters, so the iterative method is used to solve it.

3 Kinematics and dynamics simulation in different driving states

To study the road load of tracked vehicles under different driving conditions, Eq. 30 is applied to perform kinematic/dynamic simulations on the tracked vehicles and the parameters of the viscous soil conditions by using the MATLAB programming environment.

When the weight of the vehicle is 38 tons, the width of the vehicle is 3.5 m, the radius of the driving wheel is 0.286 m, the height of the center of mass is 1.25 m, the track length is 5 m, and the track width is 0.4 m, then we have: $k_c = 13.19\ kN \cdot m^{n+1}$; $k_\varphi = 692.5\ kN \cdot m^{n+2}$; $n = 0.5$; $E_1 = 0.44$; $E_2 = 20$.

3.1 The impact of inclination angle and steering angle on vehicle kinematics

Assuming that the vehicle speed remains at 3 m/s and the steering radius remains at 30 m, the kinematic states of the vehicle are shown in Figures 6A–E as the inclination angle γ and the steering angle θ change.

From Figure 6A, it can be seen that when the vehicle is in the $\theta = 0$ position, as the inclination angle γ gradually increases, the

10.3389/fmats.2023.1188411

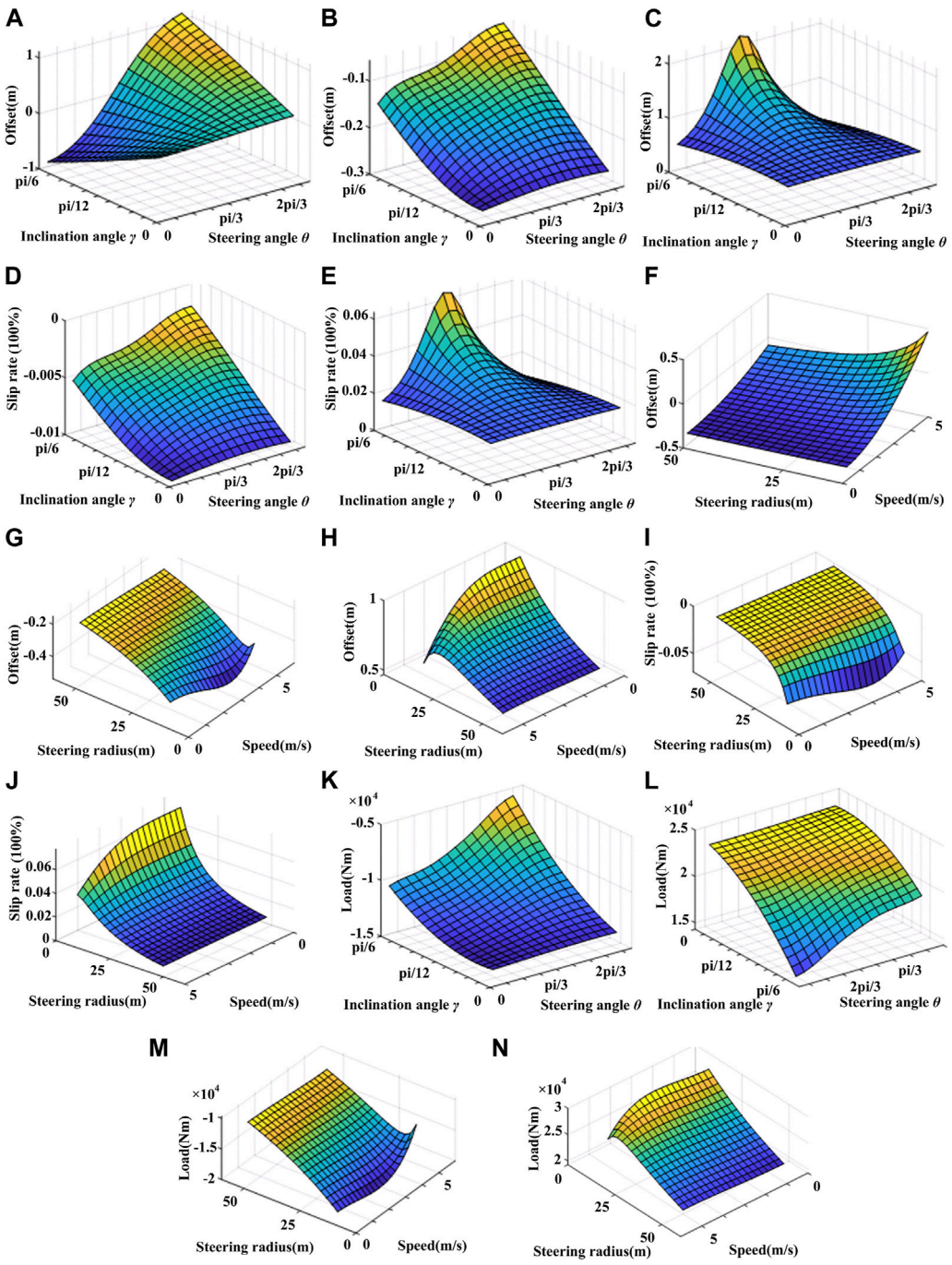

FIGURE 6
(A) Longitudinal offset of the turning center under different inclination angles and steering angles; **(B)** Instantaneous lateral offset of the turning center of the inner trackunder different inclination angles and steering angles; **(C)** Instantaneous lateral offset of the turning center of the outer trackunder different inclination angles and steering angles; **(D)** Ground slip ratio of the inner trackunder different inclination angles and steering angles; **(E)** Ground slip ratio of the outer trackunder different inclination angles and steering angles; **(F)** Longitudinal offset of the steering center under different steering radii and speeds; **(G)** Inner steering center lateral offsetunder different speeds and steering radii; **(H)** Outer steering center lateral offsetunder different speeds and steering radii; **(I)** Ground slip ratio of the inner trackunder different speeds and steering radii; **(J)** Ground slip ratio of the outer trackunder different speeds and steering radii; **(K)** Inner drive wheel loadunder different inclination angles and steering angles conditions; **(L)** Outer drive wheel loadunder different inclination angles and steering angles conditions; **(M)** Inner drive wheel loadunder different speeds and steering radii conditions; **(N)** Outer drive wheel loadunder different speeds and steering radii conditions.

longitudinal offset of the turning center gradually shifts towards the rear of the vehicle's center of gravity. This is because when γ increases, the gravity of the entire vehicle generates a backward force along the direction of vehicle travel, causing the load on the rear track of the vehicle to be greater than that on the front track, leading to a rearward shift of the turning center. As the vehicle's

steering angle increases, the longitudinal offset of the turning center is affected by the load distribution and gradually shifts towards the front of the vehicle's center of gravity, which is consistent with the vehicle's motion law.

Figures 6B, C show the lateral offset curve of the instantaneous steering center of the two tracks. For the inner track, the lateral offset of the instantaneous center of speed increases nonlinearly with the increase of the steering angle and inclination angle. For the outer track, when $\gamma = 0$, the effect of the steering angle θ on the lateral offset of the instantaneous center of speed can be neglected. However, when $\gamma > 0$, the lateral offset of the instantaneous center of speed follows a normal distribution curve, and when the vehicle's steering angle is $\frac{\pi}{2}$, the lateral offset of the instantaneous center of speed of the outer track reaches its maximum value.

By comparing Figures 6B–E, it can be seen that the ground slip ratio of the two tracks and the distribution curve of the lateral offset of the turning center of the tracks have a similar trend. The main reason for this can be obtained by analyzing Eq. 16 and Eq. 17. The combination of the two equations shows that the ground slip ratio of the track is linearly positively correlated with the lateral offset of the steering center. Therefore, the lateral offset of the steering center is the main factor affecting the ground slip ratio of the tracks.

3.2 The influence of steering radius and vehicle speed on vehicle kinematics

Assuming the vehicle is driving on a surface with a inclination angle of $\gamma = 10°$ and a steering angle of $\theta = 10°$ at a certain moment. At this time, under different steering radii and vehicle speeds, the kinematic state of the vehicle is shown in Figures 6F–J.

From Figure 6F, it can be seen that at different steering radii, as the vehicle speed increases, the longitudinal offset of the vehicle's steering center moves forward, because the vehicle needs to move the steering center forward to match the gradually increasing centrifugal force, which conforms to the laws of vehicle kinematics.

The influence of vehicle speed and steering radius on the lateral offset of the instantaneous steering center of the tracks is shown in Figures 6G, H. It can be seen from the figure that the absolute value of the lateral offset of the instantaneous steering center of both tracks is negatively correlated with the vehicle steering radius, and when the vehicle steering radius is large, the lateral offset of the steering center is not sensitive to changes in vehicle speed. This is because when the vehicle is making a large-radius turn, the difference in load between the two tracks decreases, and when the vehicle's steering radius approaches infinity, the vehicle travels in a straight line.

Figures 6I, J shows the variation curves of instantaneous track slip ratios under different vehicle speeds and steering radii. As can be seen from Figure 6I, if the steering radius remains unchanged, the vehicle speed has a small effect on the slip ratio, and the slip ratio of the inner track increases gradually as the steering radius decreases. By comparing Figures 6I, J, it can be found that the vehicle speed only has a significant effect on the slip ratio under low steering radius conditions. This is because as the steering radius of the vehicle increases, the trajectory of the entire vehicle tends to be more straight-line movement. This phenomenon conforms to the laws of vehicle motion.

3.3 The impact of inclination angle and steering angle on vehicle dynamics

As shown in Figures 6K, L, it can be seen that during vehicle operation, the load on the inner driving wheel is positively correlated with the inclination angle and steering angle, while it is negatively correlated with the load on the outer driving wheel. This is mainly because as the inclination angle and steering angle of the vehicle increase, the center of gravity of the vehicle gradually shifts towards the inner track, causing an increase in the vertical load on the inner track.

3.4 The influence of steering radius and speed on vehicle dynamics

The impact of vehicle speed and steering radius on the load of the two driving wheels is shown in Figures 6M, N. As shown in Figures 6M, N, when the steering radius of the vehicle increases, the vehicle tends to travel in a straight line, and the absolute value of the load on both sides of the wheels gradually decreases. When the steering radius of the vehicle is constant and the speed increases, due to the change of centrifugal force, the absolute value of the load on both sides of the wheels decreases in a parabolic shape. Moreover, when the steering radius of the vehicle increases, the impact of speed on the load of the vehicle gradually decreases.

4 The inertia transfer phenomenon during the load simulation process

In actual driving, the load on the two sides of a heavy-duty vehicle is not the same and changes dynamically due to the vehicle's own driving and transmission system characteristics as well as the external road environment. For the load simulation system, the load motor on one side applies a load to the tested vehicle, which is also affected by the corresponding output torque of the output shaft and the simulated ground environment. Therefore, one of the key points to achieve accurate whole vehicle load simulation is to dynamically allocate the load and inertia required to be simulated to the load simulation motors corresponding to each driving axle through dynamic allocation, and each load simulation motor then implements the vehicle load simulation using the single axle load simulation method (Bekker, 1960).

For simple load simulations, such as straight driving, the simplest method is to evenly distribute the load and inertia of the tested vehicle to each axle, and the vehicle's speed can also be directly obtained based on the speed of each axle. However, straight driving is just a special case of vehicle operation. During acceleration, braking, turning and other actions, different load distributions on both sides, turning radii, and driving speeds will occur. Therefore, in simulating the entire vehicle, evenly distributing the road load and inertial load on each side of the vehicle will inevitably result in accuracy errors in load simulation, and it is necessary to correct it by properly distributing the vehicle load.

During the load simulation process, the simulated load of the load simulation system is obtained by considering the vehicle's dynamic model and the external forces acting on the vehicle.

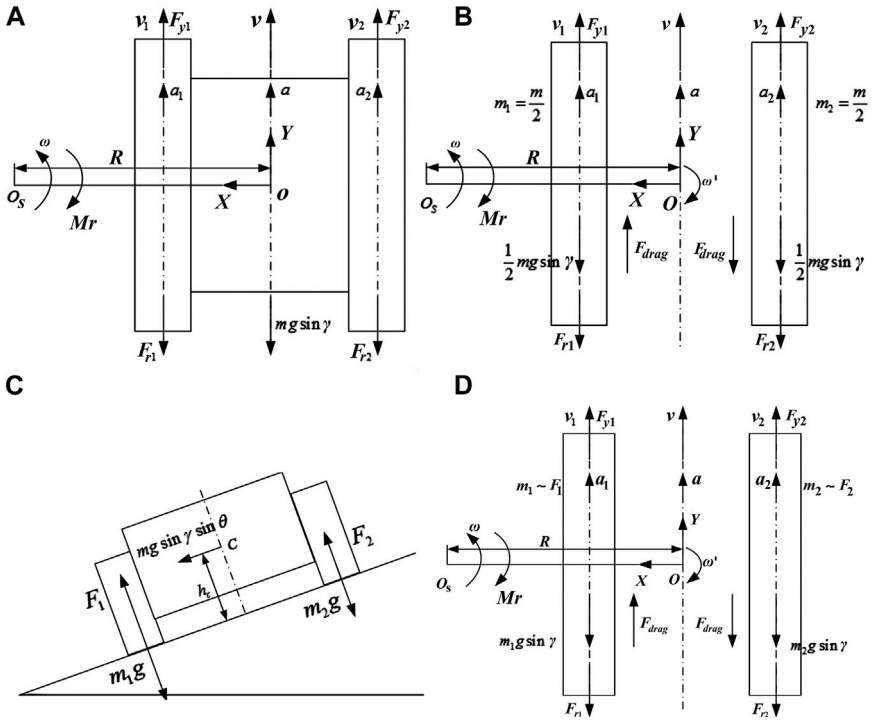

FIGURE 7
(A) The force analysis of a stable condition with the same load on both sides; **(B)** The force analysis of an unstable condition with the same load on both sides; **(C)** Analysis of forces with different loads on both sides; **(D)** Analysis of forces with different loads on both sides on unsteady-state condition.

When the external environment of the vehicle changes, the load on the left and right wheels also changes accordingly, and this load change is reflected on the test bench in the form of changes in the road load and inertia load. In the previous section, this paper obtained the vehicle's road load model. In this section, the allocation of inertia load is discussed in depth.

4.1 Steady-state conditions with equal load on both sides

For vehicle driving, steering is a universal situation that can be used to describe the driving state of the vehicle in different environments and conditions. Straight-line driving of the vehicle is a special case of the vehicle's steering driving, which can be described as the driving condition when the steering radius $R \rightarrow \infty$. For the stable condition where the loads on both sides are equal, the force on the vehicle is shown in Figure 7A. This condition often occurs during stable straight-line driving of the vehicle on a horizontal road and during low-speed turning with a large radius.

In the figure, let the instantaneous velocity direction of the vehicle be the Y direction and the direction of the line connecting the vehicle's center of mass and the turning center be the X direction. Since the load on both sides is the same and the velocity is the same, it can be deduced that the driving forces of the left and right tracks are $F_{y1} = F_{y2}$. Therefore, the driving forces of the two active wheels on both sides are $T_{e1} = T_{e2}$. Let J_{equ1} and J_{equ2} be the equivalent inertia on the left and right active wheels, respectively. At this point, since the acceleration on both sides is the same, $a_1 = a_2$, it can be obtained as:

$$\frac{T_{e1}}{J_{equ1}} = \frac{T_{e2}}{J_{equ2}} \tag{32}$$

It can be further deduced that $J_{equ1} = J_{equ2} = \frac{1}{2}J_{equ}$, where J_{equ1}、J_{equ2} represent the equivalent inertia on the left and right sides of the vehicle respectively.

4.2 Unsteady-state conditions with equal load on both sides

When the vehicle is traveling in a straight line on a horizontal surface or during low-speed turning, assuming that at a certain moment, one side of the ground contact surface slips. At this time, the coefficient of adhesion of the ground changes, and the single-side ground adhesion force cannot provide sufficient driving force. In order to investigate the load situation of the driving wheel under the conditions of the entire vehicle and side-by-side, the entire vehicle is divided into two parts, left and right, and these two parts are connected in the Y direction through a pair of equal and opposite original forces F_{drag}, which is called transfer force. As shown in Figure 7B.

Based on the above figure, in the vehicle coordinate system, the second law of Newton in the Y direction and the steering direction are as follows:

$$F_{y1} + F_{y2} - F_{r1} - F_{r2} - mgsin\gamma = ma \tag{33}$$

$$F_{y1}\frac{B}{2} - F_{y2}\frac{B}{2} - Mr = J_o\dot{\omega} \tag{34}$$

At this point, it can be reasonably assumed that the vehicle is designed such that $m_1 = m_2 = \frac{m}{2}$ when the vehicle is not subject to any lateral forces. Applying Newton's second law in the Y direction to each of these separated parts:

$$\begin{cases} F_{y1} - mgsin\gamma - F_{r1} - F_{drag} = m_1 a_1 \\ F_{y2} - mgsin\gamma - F_{r2} + F_{drag} = m_2 a_2 \end{cases} \tag{35}$$

In the equation, a_1 and a_2 satisfy:

$$a_1 = \left(1 - \frac{B}{2R}\right)a \tag{36}$$

$$a_2 = \left(1 + \frac{B}{2R}\right)a \tag{37}$$

According to Eqs. 33–37, We can get the result:

$$F_{drag} = \frac{\left(F_{y1} - F_{y2}\right)}{2} - \frac{\left(F_{r1} - F_{r2}\right)}{2} - \frac{\left(F_{y1} + F_{y2} - F_{r1} - F_{r2} - mgsin\gamma\right)B}{4R} \tag{38}$$

Where $F_{y1} = min\ (F_{y1}, F_{\varphi 1}) F_{y2} = min\ (F_{y2}, F_{\varphi 2})$, $F_{\varphi i}$ is the maximum adhesion force that the ground can provide.

That is:

$$F_{y2} \neq F_{y1} - F_{r1} + F_{r2} - \frac{\left(F_{y1} + F_{y2} - F_{r1} - F_{r2} - mgsin\gamma\right)B}{2R} \tag{39}$$

When $F_{drag} \neq 0$, F_{drag} can be viewed as an inertial force, then its corresponding virtual mass is:

$$m_{drag} = \frac{F_{drag}}{a} = \frac{m\left(F_{y1} - F_{y2} - F_{r1} + F_{r2}\right)}{2\left(F_{y1} + F_{y2} - F_{r1} - F_{r2} - mgsin\gamma\right)} - \frac{mB}{4R} \tag{40}$$

This shows that under certain driving conditions and ground adhesion conditions, the equivalent inertia of the vehicle may be distributed unequally. When the condition in Eq. 39 is satisfied, for a certain active wheel, the transfer force F_{drag} from the other side can be replaced by an equivalent mass change m_{drag} expressed by Eq. 40. For the equivalent inertia of the vehicle on both sides at this time, Eq. 41 can be obtained by introducing the equation for equivalent inertia transformation of the vehicle, as follows:

$$\begin{cases} J_{equ1} = \dfrac{\left(\frac{m}{2} + m_{drag}\right)v^2 + 2J_{tequ1} + 2J_{oequ1}}{\omega_{d1}^2} \\ J_{equ2} = \dfrac{\left(\frac{m}{2} - m_{drag}\right)v^2 + 2J_{tequ2} + 2J_{oequ2}}{\omega_{d2}^2} \end{cases} \tag{41}$$

4.3 Steady-state conditions with unequal load on both sides

When the vehicle is moving on a slope or when the position of the vehicle's center of gravity changes, the supporting forces acting on the wheels/tracks on both sides of the vehicle by the ground are not equal, as shown in Figure 7C. According to Eq. 38, it can be known that when the acceleration on both sides of the vehicle satisfies certain conditions and plus $F_{drag} = 0$, there is no transfer force internally. At this time, the equivalent inertia of the active wheels on both sides is only related to the vertical load of the active wheels on both sides.

The calculation based on Eq. 19 suggests that the equivalent masses acting on the wheels on both sides of the vehicle are:

$$\begin{cases} m_1 = \dfrac{mF_1}{F_1 + F_2} = \dfrac{\frac{mgcos\gamma}{2} + \frac{h_c}{B}\left(mgsin\gamma\, sin\,\theta - \frac{mv^2\, cos\,\theta_s}{R}\right)}{gcos\gamma} \\ m_2 = \dfrac{mF_2}{F_1 + F_2} = \dfrac{\frac{mgcos\gamma}{2} - \frac{h_c}{B}\left(mgsin\gamma\, sin\,\theta - \frac{mv^2\, cos\,\theta_s}{R}\right)}{gcos\gamma} \end{cases} \tag{42}$$

After calculation of Equivalent inertia, we have:

$$\begin{cases} J_{equ1} = \dfrac{m_1 v^2 + 2J_{tequ1} + 2J_{oequ1}}{\omega_{d1}^2} \\ J_{equ2} = \dfrac{m_2 v^2 + 2J_{tequ2} + 2J_{oequ2}}{\omega_{d2}^2} \end{cases} \tag{43}$$

4.4 Unsteady-state conditions with unequal load on both sides

During the vehicle's operation, its behavior is affected by the driver's driving behavior, which belongs to a pseudo-random working condition. At the same time, the ground conditions for vehicle operation are influenced by soil composition, water content, and terrain, resulting in different ground adhesion forces on both sides of the vehicle. Therefore, when considering the equivalent inertia of both sides, not only the distribution of vertical loads but also the variation of the internal transfer force F_{drag} on the inner side must be considered. At this point, due to the different loads on both sides of the vehicle, the forces acting on the two separate bodies of the vehicle are shown in Figure 7D.

In Figure 7D, m_1、m_2 can be calculated through Eq. 42. Apply Newton's second law to these two separate bodies in the Y direction respectively:

$$\begin{cases} F_{y1} - m_1 gsin\gamma\, cos\,\theta - F_{r1} - F_{drag} = m_1 a_1 \\ F_{y2} - m_2 gsin\gamma\, cos\,\theta - F_{r2} + F_{drag} = m_2 a_2 \end{cases} \tag{44}$$

According to Eq. 38, We can get the result:

$$F_{drag} = \frac{\left(F_{y1} - F_{y2}\right) - \left(F_{r1} - F_{r2}\right) - (m_1 - m_2)gsin\gamma\, cos\,\theta - (m_1 a_1 - m_2 a_2)}{2} \tag{45}$$

Which also means:

$$F_{y2} \neq F_{y1} - \left(F_{r1} - F_{r2}\right) - (m_1 - m_2)gsin\gamma\, cos\,\theta - (m_1 a_1 - m_2 a_2) \tag{46}$$

When $F_{drag} \neq 0$, its corresponding virtual mass is:

$$m_{drag} = \frac{\left(F_{y1} - F_{y2}\right) - \left(F_{r1} - F_{r2}\right) - (m_1 - m_2)gsin\gamma\, cos\,\theta - (m_1 a_1 - m_2 a_2)}{2a} \tag{47}$$

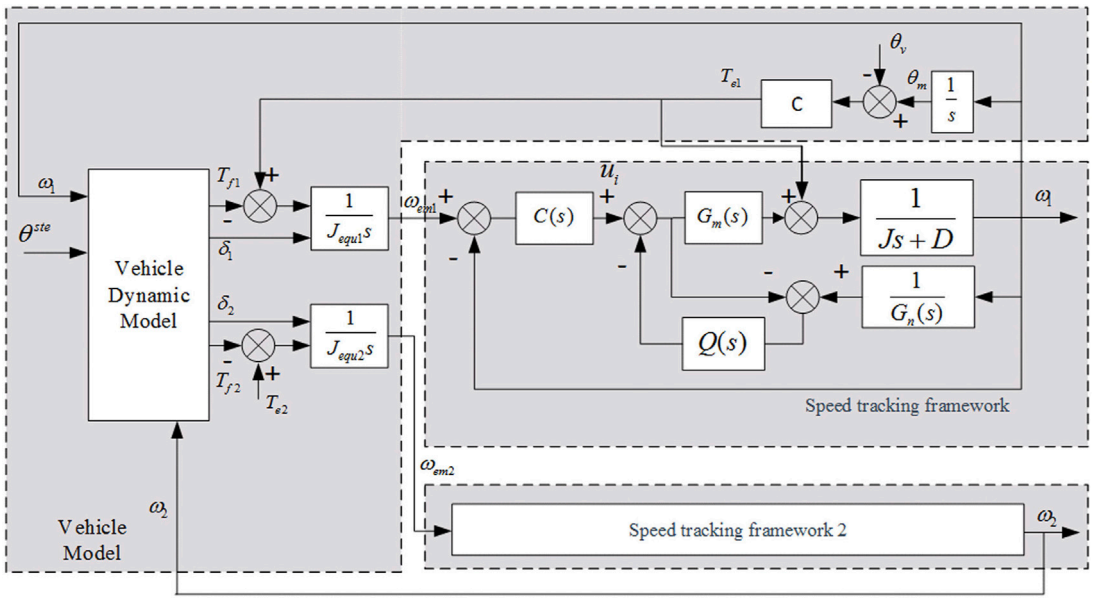

FIGURE 8
Control diagram of load simulation system under non-uniform speed and non-uniform load conditions.

In the same way, the equivalent inertia on both sides can be obtained as:

$$\begin{cases} J_{equ1} = \dfrac{\left(m_1 + m_{drag}\right)v^2 + 2J_{tequ1} + 2J_{oequ1}}{\omega_{d1}^2} \\ J_{equ2} = \dfrac{\left(m_2 - m_{drag}\right)v^2 + 2J_{tequ2} + 2J_{oequ2}}{\omega_{d2}^2} \end{cases} \tag{48}$$

Through the study of vehicle equivalent inertia distribution, this section establishes a model of equivalent inertia distribution as described in Eq. 32, Eq. 41, Eq. 43, and Eq. 48. By studying the inertial load, errors in load simulation caused by uneven distribution of inertial load are avoided.

5 Whole vehicle load simulation control and its synchronization error compensation

Through the derivation in Section 4.2, the inertia load model of the whole vehicle under different driving conditions can be obtained. Based on these models, to further obtain the target speed of the vehicle, it is necessary to know the current driving wheel speed ω_i (i = 1,2, etc.), the current torque T_{ei}, and the current target steering radius R. Among them, ω_i and T_{ei} can be obtained through sensors, while R needs to be obtained through an angle displacement sensor installed on the steering wheel.

During vehicle operation, the steering wheel reflects the driver's steering demand. When the steering wheel angle θ^{ste} is within the free travel range $(-\theta_0^{ste}, +\theta_0^{ste})$, the vehicle maintains straight-line driving. When $|\theta^{ste}| > \theta_0^{ste}$, the vehicle turns. The target steering speed of the vehicle can be represented by angular velocity ω^{ste}. The maximum steering angle of the steering wheel $\pm\,\theta_{max}^{ste}$ corresponds to the maximum steering angular velocity ω_{max}^{ste} on the left and right sides of the vehicle. The mapping relationship between the steering wheel angle and the vehicle angular velocity is:

$$\omega^{ste} = \frac{\theta^{ste} - \theta_0^{ste}}{\theta_{max}^{ste} - \theta_0^{ste}} \cdot \omega_{max}^{ste} \tag{49}$$

The relationship between the vehicle linear velocity v_v, the target steering radius R, and the angular velocity ω^{ste} can be obtained through the arc length equation:

$$\frac{v_v}{R} = \omega^{ste} \tag{50}$$

Therefore, through the vehicle's steering wheel angle signal, the driving wheel speed signal, and the current ground slip ratio, the target steering radius of the vehicle at the next moment can be known. By introducing these parameters into the vehicle dynamics model and combining them with the vehicle equivalent inertia model, the control model of the whole vehicle load simulation can be obtained, as shown in Figure 8.

5.1 Cross-coupling compensation under the condition of equal speeds on both sides

In the control process of the entire vehicle load simulation, each side's driving wheel corresponds to a set of load simulation systems (referred to as subsystems below), and all subsystems receive instructions from the same control system to simulate the loads of each wheel, thereby achieving the load simulation of the entire vehicle. Therefore, there is also a problem of multi-motor synchronization control in the control of the entire vehicle load

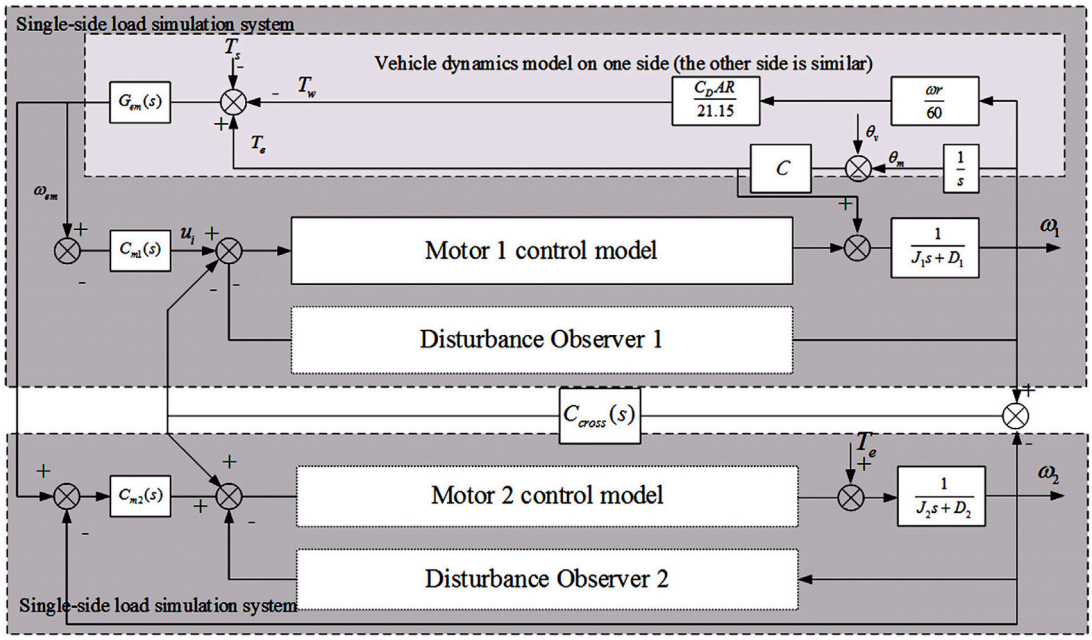

FIGURE 9
Cross-coupling compensation of the load simulation system under the condition of the same driving wheel speed.

simulation system. In the process of multi-motor synchronization control, the differences in hardware and mechanics between the various independent subsystems make it difficult for the control system to keep the controlled variables of each motor in a linear relationship, resulting in synchronization errors. To solve this problem, this section takes the track-type vehicle load simulation system as an example and uses the idea of cross-coupling compensation to compensate for the deviation between the two motors.

The basic principle of compensation correction is to detect the synchronization error ε of the speed ω_i and compensate it through the correction operation of the controller $C_{cross}(s)$. If the synchronization position error $\varepsilon > 0$, it means that $\omega_1 > \omega_2$. At this time, a negative compensation value is applied to the speed loop of motor 1, and a positive compensation value is applied to the speed loop of motor two to quickly reduce the error between the two motors. If the synchronization position error $\varepsilon < 0$, the situation is completely opposite. The cross-coupling controller $C_{cross}(s)$ adopts a PI controller. Since the speed deviation between the motors is relatively small compared to the motor speed, in order to make ε converge quickly, the PI controller is designed through repeated experiments as follows:

$$C_{cross}(s) = \frac{2.2s + 15}{s} \tag{51}$$

The resulting framework for the overall vehicle control under straight-line driving can be obtained as shown in Figure 9.

A certain heavy-duty vehicle is subjected to dual-side load simulation. A virtual dashed line is used to indicate the enlarged position where a momentary torque disturbance of 500 Nm is applied to the left load simulation system. The simulation results are shown in Figure 10A. At $t = 14$s, the deviation of the left and right drive wheel speeds without considering cross-coupling compensation is about 0.3 rad/s. After taking cross-coupling compensation into consideration, both sides of the load simulation system generates a speed fluctuation of about 0.15 rad/s, but the relative speed deviation between the left and right sides has been reduced to 0.04 rad/s, and the synchronization of the system has been significantly improved.

A certain heavy-duty vehicle has been subjected to load simulation, and a system delay of 0.1s is given to the left-side load simulation system during the 10th second of the simulation. The simulation results are shown in Figure 10B. After the change of driving torque, due to the delay of the left-side system, there is a significant difference in the speed curves of the two sides, and the maximum value of the speed deviation at the same time is about 1.20 rad/s, which maintains a speed deviation of 0.38 rad/s after the speed fluctuation stabilizes. After considering the cross-coupling compensation, the maximum speed deviation drops to 0.24 rad/s, and quickly converges to 0, and the synchronization of the system is significantly improved.

5.2 Cross-coupling compensation under different speeds on both sides

Under the experimental conditions where the speeds on both sides are different, introducing Eq. 42 into Figure 8 yields the system control framework under different speed conditions, as shown in Figure 11. Unlike the cross-coupling compensation under straight-line driving conditions, since the speeds on both sides are different, it is necessary to first calculate the vehicle's driving speed v using the

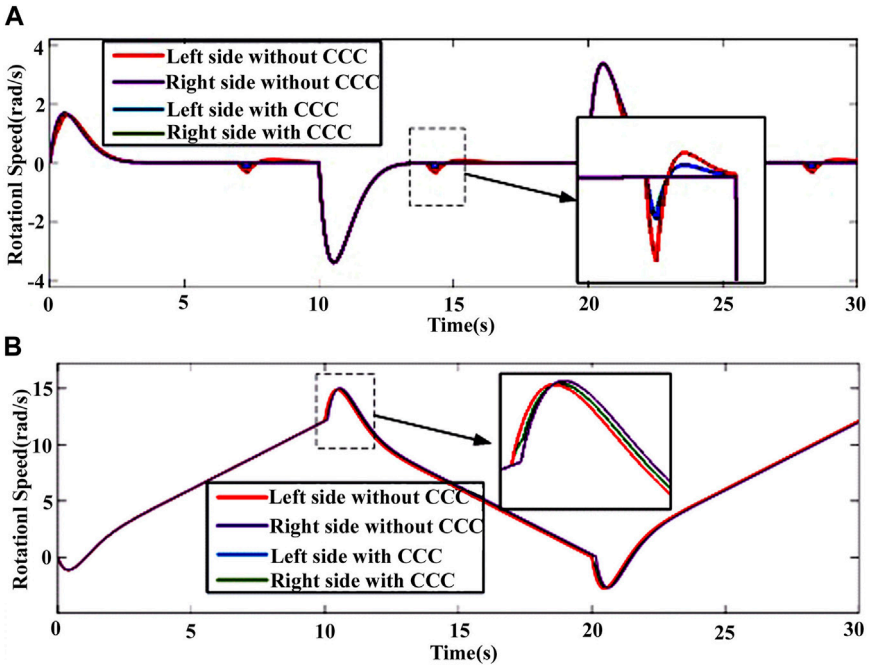

FIGURE 10
(A) Simulation curve of vehicle straight driving considering CCC (CCC is short for Cross-coupling compensation) under single-side pulse disturbance condition; **(B)** Simulation curve of vehicle straight driving considering CCC under single-side delay error condition.

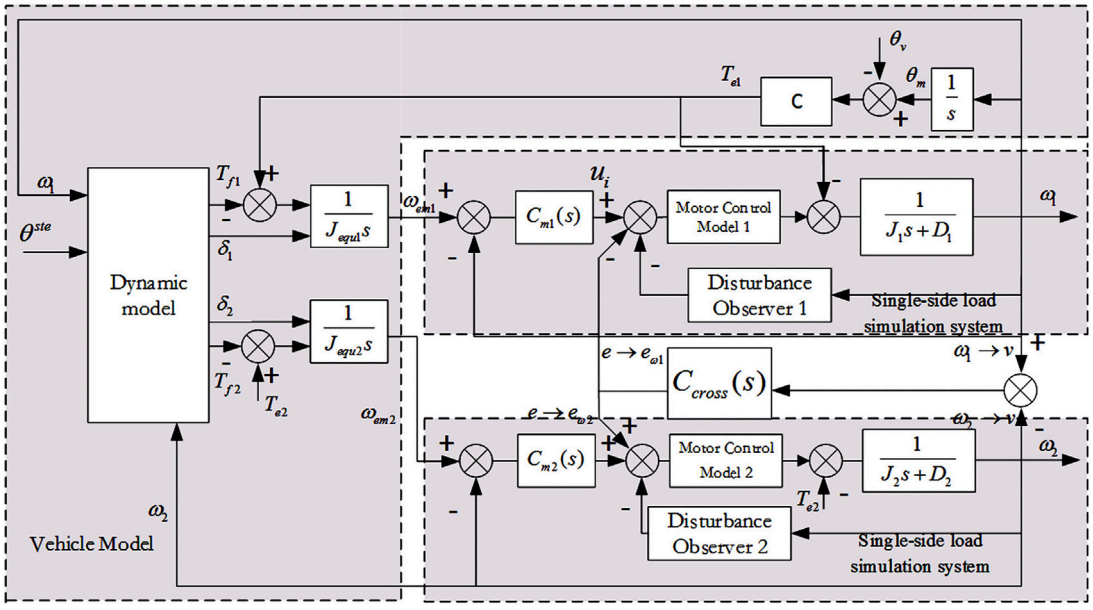

FIGURE 11
Cross-coupling compensation under different driving wheel speeds.

speeds ω_i on both sides and then proceed with the cross-coupling compensation.

The same vehicle has been subjected to load simulation under steering conditions, with a uniform acceleration rotation of radius 50 m on a circular ramp with a slope of 10°. The speed response of both sides is shown in Figure 12.

As shown in Figure 12A, a disturbance with a pulse torque amplitude of 2000 Nm has been applied to the inner load simulation

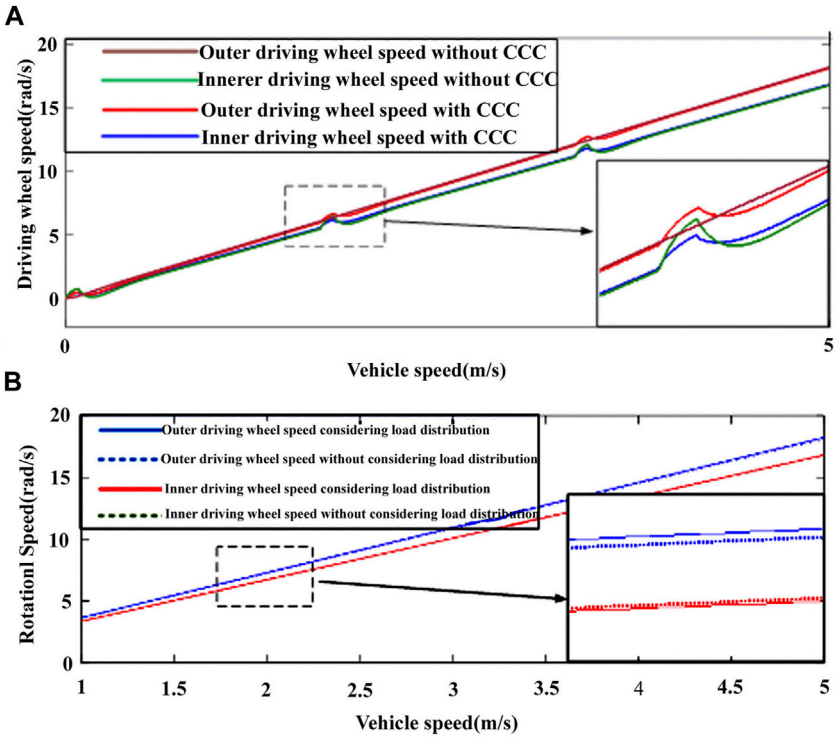

FIGURE 12
(A) Vehicle speed response under steering conditions; **(B)** Speed response of vehicle with consideration of CCC under steering condition.

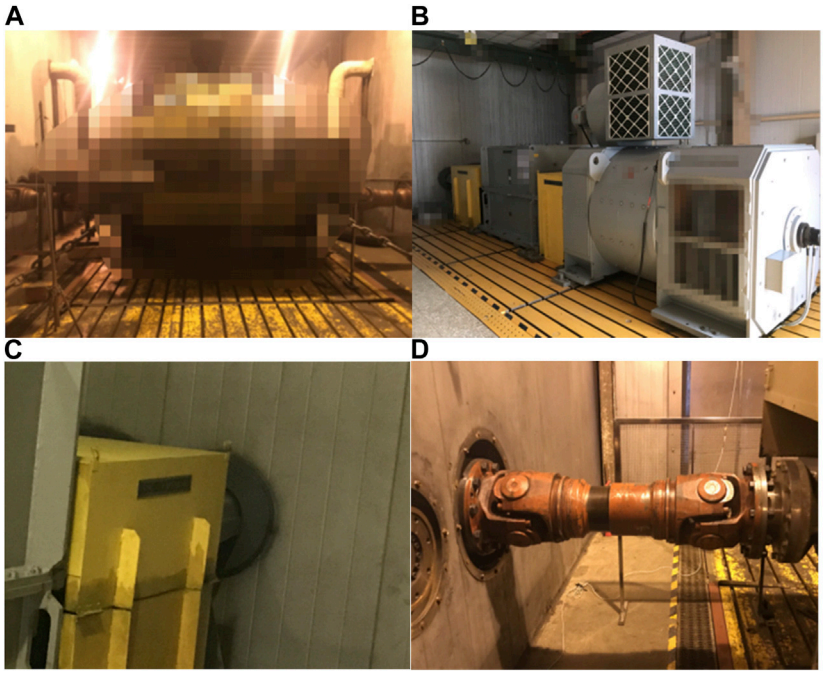

FIGURE 13
Mechanical structure of simulation device: **(A)** Environmental chamber; **(B)** Single-sided power compartment; **(C)** Through-wall shaft power compartment end; **(D)** Through-wall shaft environmental chamber end.

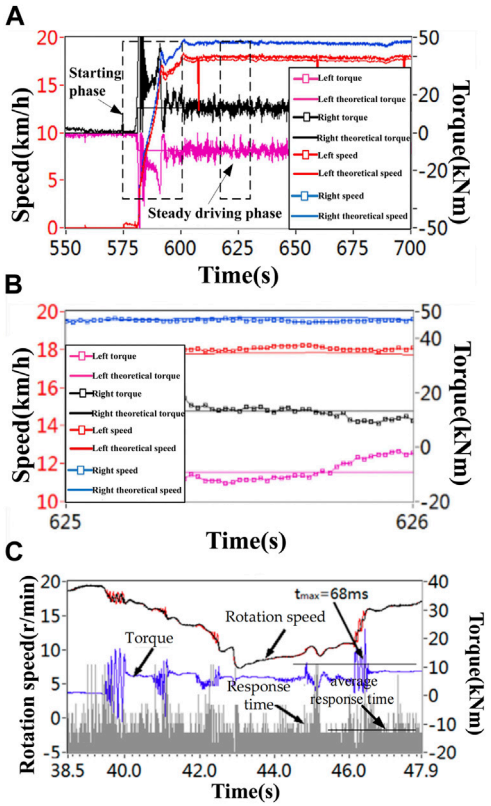

FIGURE 14
Load steering test: **(A)** Overall test data; **(B)** Amplified portion of data during stable driving phase; **(C)** System response time.

system, resulting in a speed fluctuation amplitude of 0.64 rad/s in the inner load simulation system due to the disturbance rejection effect of the disturbance observer. After taking the cross-coupling compensation into consideration, the outer speed fluctuates together with the inner speed, and the amplitude of the inner speed fluctuation decreases to 0.28 rad/s. The equivalent speed deviation between the two sides also decreases to 0.13 rad/s and quickly converges to 0. The synchronization of the system has been significantly improved.

As shown in Figure 12B, the speed response curve considering load distribution and slip ratio has a significant difference from the speed response curve without considering these factors. When the vehicle speed is 5 m/s, the inner speed response considering load distribution is 16.81 rad/s, and the speed response without considering load distribution is 16.98 rad/s, with a deviation of 1.01%. The outer speed response considering load distribution is 18.24 rad/s, and the speed response without considering load distribution is 17.95 rad/s, with a deviation of 1.58%.

6 Experimental technique analysis

The heavy-duty vehicle load simulation test bench mainly consists of a load simulation system and the test vehicle, and the test vehicle must be separated and enclosed in the environmental chamber to simulate various driving environments. Power compartments with load simulation motors and transmission mechanisms installed are located on both sides of the environmental chamber, as shown in Figures 13A, B. The transmission mechanism of the power compartment and the test vehicle inside the environmental chamber are connected through a through-wall shaft, as shown in Figures 13C, D. To prevent salt spray, sand, and other debris from entering the bearings, the walls at both ends of the through-wall shaft are mechanically sealed.

In this structure, by combining torque signals with the actual vehicle dynamics model, the target speed of the driving wheel and the speed of the high-power motor in the power compartment can be calculated, thereby achieving the goal of subjecting the driving wheel of the tested vehicle to the same load as the actual road driving (Fajri et al., 2012). The mechanical architecture of shaft coupling also ensures that the simulated loads between each subsystem are independent of each other, thus enabling the entire system to achieve composite working condition load simulation at the structural level.

During the testing process, the system controller needs to simultaneously control, calculate, and acquire data from both the test bench and the environmental chamber. As real-time calculations and motor control for both road load and inertial load are required during the testing process, the test system adopts a two-layer real-time control method for solving and controlling the load simulation system. During the testing process, the test management computer is responsible for managing, controlling, and displaying the testing project, and sends commands to the real-time control computer and PLC. The PLC is responsible for controlling the environmental simulator and collecting environmental signals to provide feedback to the test management computer. Two closed loops are formed between the real-time control computer and the electric motor, where the upper loop acquires the vehicle speed and steering signals and calculates/updates the real-time vehicle speed based on the whole vehicle kinematics model before sending it to the lower layer controller. The lower loop realizes the speed tracking control of each motor.

The control method of the single-side load simulation device that we use is speed tracking. During system operation, the board collects the steering angle signal θ^{ste} and outputs the speed ω and torque T_e. Based on the dynamic model calculation method described in Eq. 30 and the equivalent inertia model (32), (41), (43), and (48) of the heavy-duty vehicle, the vehicle's load model is derived to obtain the target speed ω_{em} of the vehicle. In the time

TABLE 1 Experimental data for load steering test during stable driving phase.

Simulated object	Theoretical speed (km/h)	Measured speed (km/h)	Error (%)	Theoretical torque (kNm)	Measured torque (kNm)	Error (%)
Left-side wheel	18.03	17.77	1.48	9.22	9.43	2.25
Right-side wheel	19.63	19.52	0.54	13.17	13.29	0.87

domain, the speed tracking module calculates the torque command $u_i(n+1)$ for simulating the inertia load and road load of the test vehicle based on the next stage target speed $\omega_{em}(n+1)$, the output speed $\omega(n)$ obtained by the sensor, and the feedback torque $T_e(s)$ from the torque sensor. After motor control, the target speed is output to achieve load simulation of the single-side driven wheel.

Load steering test is a test that studies the torque and speed during vehicle steering process. Through load steering test, the load condition of vehicle transmission equipment under steering conditions can be studied. For the test bench itself, the accuracy of simulating vehicle load steering can be verified through the test.

Figure 14 shows the test data of simulating a vehicle with a curb weight of 30t, turning left at a constant speed on a level ground with a radius of 50 m and a speed of 18 km/h. Due to the influence of the driver's behavior on the driving speed of the vehicle, the measured stable driving speed of the vehicle is approximately 18.5 km/h. To determine the system response time under the preset spectrum, the experiment first verifies the system response time. According to Figure 14C, the average response time of the system is 25.40 m. The slowest response of the system torque occurs during several periods of significant torque fluctuations, during which the system speed fluctuates repeatedly. Due to system lag, the system is unable to respond in a timely manner, with a maximum response time of 68 m.

As shown in Figure 14A, during the startup phase, when the vehicle accelerates, the torque of the load motor fluctuates repeatedly to match the theoretical speed of the vehicle due to the response delay of the equipment. When the equipment enters the stable driving stage, as shown in Figure 14B, the theoretical values and the measured values of the left and right load simulation equipment are shown in Table 1.

Based on the data in Table 1, it can be seen that the error in both the speed and torque of the left-side load simulation equipment is higher than that of the right-side equipment, which is due to sampling errors in the torque and speed sensors on the left side. As there is a problem of asynchronous loading on the left and right sides during the steering simulation test, the internal load and speed on both sides may affect each other during the load simulation process. From Figure 14 and Table 1, it can be seen that the overall error of the equipment in the steering simulation process is less than 2.5%, indicating that the experimental platform designed in this paper can achieve accurate steering load simulation.

7 Conclusion

This paper studies the load simulation method for tracked vehicles under complex working conditions, based on the control strategy of single-axis load simulation system and the dynamic model of tracked vehicle during turning process. Firstly, the equivalent inertia allocated to the two wheels in different driving conditions are obtained through in-depth research on load allocation of vehicles under different driving conditions. To address the issue of synchronization errors in the motor during the complex working condition tests, the cross-coupling compensation method is used to reduce the synchronization errors. The experimental results show that the load simulation system considering equivalent inertia allocation and cross-coupling compensation has higher simulation accuracy and lower synchronization errors, and achieves accurate and engineering-meaningful load simulation for heavy-duty vehicles at the theoretical level.

Data availability statement

The original contributions presented in the study are included in the article/Supplementary Material, further inquiries can be directed to the corresponding authors.

Author contributions

HL conceived the overall structure and framework of the article. GL conceived the outline of the manuscript. HL and GL wrote the manuscript and generated the figures. WC and JM helped to perform the manuscript with constructive discussions. In the process of revising the paper, ZC has made important contributions to the change of the overall framework and technical route of the paper. All authors contributed to the article and approved the submitted version.

Conflict of interest

Authors HL and JM were employed by the company Suzhou Sc-Solar Equipment Co., Ltd.

The remaining authors declare that the research was conducted in the absence of any commercial or financial relationships that could be construed as a potential conflict of interest.

Publisher's note

References

Bai, J., Wu, X., Gao, F., Li, H., and Yue, H. (2017). Modeling and simulation of multi-axle vehicle powertrain system[J]. *J. Beijing Univ. Aeronautics Astronautics* 43 (1), 136–143. doi:10.13700/j.bh.1001-5965.2016.0708

Bekker, M. G. (1960). *Off-road locomotion: Research and development in terramechanics*. Ann Arbor, Michigam: The Univ of Michigam press.

ChenZhouWang, Z. X. Z., Li, Y., and Hu, B. (2019). A novel emergency braking control strategy for dual-motor electric drive tracked vehicles based on regenerative braking. *Appl. Sci.* 9 (12), 2480. doi:10.3390/app9122480

Fajri, P., Ahmadi, R., and Ferdowsi, M. (2012). "Equivalent vehicle rotational inertia used for electric vehicle test bench dynamic studies[C]," in Proceedings of the 38th IEEE

Industrial Electronics Society Annual Conference, 25-28 October 2012 (Montreal, QC, Canada: IEEE), 4115–4120.

Fajri, P., Ahmadi, R., and Ferdowsi, M. (2013). "Test bench for emulating electric-drive vehicle systems using equivalent vehicle rotational inertia[C]," in 2013 IEEE Power and Energy Conference at Illinois (PECI), Urbana, IL, USA, 22-23 February 2013 (IEEE), 83–87.

Fu, W. X., Sun, L., Yu, Y. F., Zhu, S. P., and Yan, J. (2009). Design and model-building of motor-driven load simulator with large torque outputs[J]. *J. Syst. Simul.* 21, 3596–3598.

Huh, K., Kim, J., and Hong, D. (2001). "Estimation of dynamic track tension utilizing a simplified tracked vehicle model [C]," in Proceedings of the American Control Conference, Arlington, VA, USA, 25-27 June 2001 (IEEE), 25–27.

Janarthanan, B., Padmanabhan, C., and Sujatha, C. (2011). Lateral dynamics of single unit skid-steered tracked vehicle. *Int. J. Automot. Technol.* 12 (6), 865–875. doi:10.1007/s12239-011-0099-4

Jiang, F., Dong, M., Fan, Y., and Wang, Q. (2022). Research on motor speed control method based on the prevention of vehicle rollover[J]. *Energies* 15, 3609. doi:10.3390/en15103609

Kim, J. H., Park, C. S., Kim, S. G., and Kim, J. H. (2003). Hydraulic system design and vehicle dynamic modeling for the analysis and development of tire roller[J]. *Int. J. Control Autom. Syst.* 1, 89–94.

Lv, H., Zhou, X., Yang, C., Wang, Z., and Fu, Y. (2019). Research on the modeling, control, and calibration technology of a tracked vehicle load simulation test bench. *Appl. Sci.* 9 (12), 2557. doi:10.3390/app9122557

Nam, Y. (2001). QFT force loop design for the aerodynamic load simulator. *IEEE Trans. Aerosp. Electron. Syst.* 37 (4), 1384–1392. doi:10.1109/7.976973

Ott, H., Degen, R., Leijon, M., and Ruschitzka, M. (2021). Model-based approach to investigate the influences of different load states to the vehicle dynamics of light electric vehicles[J]. *Transp. Sci. Technol.* 11 (02), 213–230. doi:10.4236/jtts.2021.112014

Takeda, M., Hosoyamada, Y., Motoi, N., and Kawamura, A. (2014). "Development of the experiment platform for electric vehicles by using motor test bench with the same environment as the actual vehicle," in 2014 IEEE 13th International Workshop on Advanced Motion Control (AMC), Yokohama, Japan, 14-16 March 2014 (IEEE).

Wang, H., Song, Q., Wang, S., and Zeng, P. (2015). Dynamic modeling and control strategy optimization for a hybrid electric tracked vehicle. *Math. Problems Eng.* 2015, 1–12. doi:10.1155/2015/251906

Wang, H., and Sun, F. C. (2014). Dynamic modeling and simulation on a hybrid power system for dual-motor-drive electric tracked bulldozer. *Appl. Mech. Mater.* 494-495, 229–233. doi:10.4028/www.scientific.net/amm.494-495.229

Wang, Z., Lv, H., Zhou, X., Chen, Z., and Yang, Y. (2018). Design and modeling of a test bench for dual-motor electric drive tracked vehicles based on a dynamic load emulation method. *Sensors* 18, 1993. doi:10.3390/s18071993

Xingguo, M., Tao, Y., Xiaomei, Y., and Bin, Z. (2011). "Modeling and simulation of multibody dynamics for tracked vehicle based on RecurDyn [C]," in International Conference on Intelligent Networks & Intelligent Systems, Shenyang, China, 01-03 November 2010 (IEEE).

Yalla, S. K., Kareem, A., and Asce, M. (2007). Dynamic load simulator: Actuation strategies and applications. *J. Eng. Mech.* 133, 855–863. doi:10.1061/(asce)0733-9399(2007)133:8(855)

Yang, J., Zhou, X., Wei, Y., and Gong, R. (2013). Test bed modeling and control method for track vehicle. *Trans. Chin. Soc. Agric. Mach.* 44 (06), 8–13. doi:10.6041/j.issn.1000-1298.2013.06.002

Zou, Y., Kong, Z., Liu, T., and Liu, D. (2016). A real-time Markov chain driver model for tracked vehicles and its validation: Its adaptability via stochastic dynamic programming. *IEEE Trans. Veh. Technol.* 66, 3571–3582. doi:10.1109/tvt.2016.2605449